Geophysical Research Letters

RESEARCH LETTER

10.1029/2021GL092383

Key Points:

- Spacecraft observations of magnetic cavities are sometimes accompanied by azimuthal magnetic field indicating the helical structure
- Kinetic, equilibrium model of helical magnetic cavities is developed based on four invariants of particle motion
- The model reproduces the MMS observations of helical magnetic cavities in both electromagnetic field and particle distributions

Correspondence to:

X.-Z. Zhou,
xzzhou@pku.edu.cn

Citation:

Li, J.-H., Zhou, X.-Z., Yang, F., Artemyev, A. V., & Zong, Q.-G. (2021). Helical magnetic cavities: Kinetic model and comparison with MMS observations. *Geophysical Research Letters*, *48*, e2021GL092383. https://doi.org/10.1029/2021GL092383

Received 2 JAN 2021
Accepted 8 FEB 2021

Helical Magnetic Cavities: Kinetic Model and Comparison With MMS Observations

Jing-Huan Li[1], Xu-Zhi Zhou[1], Fan Yang[1], Anton V. Artemyev[2,3], and Qiu-Gang Zong[1]

[1]School of Earth and Space Sciences, Peking University, Beijing, China, [2]Institute of Geophysics and Planetary Physics, University of California, Los Angeles, CA, USA, [3]Space Research Institute, Russian Academy of Sciences, Moscow, Russia

Abstract Magnetic cavities are sudden depressions of magnetic field strength widely observed in the space plasma environments, which are often accompanied by plasma density and pressure enhancement. To describe these cavities, self-consistent kinetic models have been proposed as equilibrium solutions to the Vlasov-Maxwell equations. However, observations from the Magnetospheric Multi-Scale (MMS) constellation have shown the existence of helical magnetic cavities characterized by the presence of azimuthal magnetic field, which could not be reconstructed by the aforementioned models. Here, we take into account another invariant of motion, the canonical axial momentum, to construct the particle distributions and accordingly modify the equilibrium model. The reconstructed magnetic cavity shows excellent agreement with the MMS1 observations not only in the electromagnetic field and plasma moment profiles but also in electron pitch-angle distributions. With the same set of parameters, the model also predicts signatures of the neighboring MMS3 spacecraft, matching its observations satisfactorily.

Plain Language Summary Magnetic cavities, also referred to as magnetic holes, are ubiquitous in the space plasma environment characterized by depressed magnetic field strength and enhanced plasma pressure. These structures are usually believed to result from plasma instabilities, although recent observations and simulations have suggested their quasi-stationary nature. Kinetic models of magnetic cavities have been also proposed, which show excellent agreement with spacecraft observations to indicate the formation of quasi-equilibrium cavities during the turbulent evolution of space plasmas. These models, however, apply only to magnetic cavities with straight field lines, and therefore cannot describe the helical magnetic cavities recently discovered by NASA's Magnetospheric Multi-Scale (MMS) constellation. In this paper, we propose a revised model by incorporating the canonical axial momentum as an additional invariant of particle motion into the particle distributions, to resolve the self-consistent profiles of the electromagnetic field and particle distributions within the magnetic cavity. This revision accommodates the field-aligned current to support the helical field lines, which shows remarkable agreement with the observations from the MMS constellation.

1. Introduction

Magnetic cavities, sometimes referred to as magnetic holes or dips, are quasi-symmetric structures in the space plasma environments with depressed magnetic field strength and enhanced plasma pressure (Haynes et al., 2015; Huang et al., 2017; Liu et al., 2019a). These structures, with size ranging from fluid to electron kinetic scales, have been observed in a variety of regions such as magnetosheath (Tsurutani et al., 2011; Yao et al., 2017; Liu et al., 2019a), magnetotail (Ge et al., 2011; Balikhin et al., 2012; Goodrich et al., 2016a; Shustov et al., 2019, 2020; Sun et al., 2012; Sundberg et al., 2015; Yao et al., 2016; Zhang et al., 2017), solar wind (Russell et al., 2008; Turner et al., 1977; Winterhalter et al., 1994; Xiao et al., 2010), heliosheath (Burlaga et al., 2006), and planetary (Cattaneo et al., 1998; Joy et al., 2006) or cometary environments (Plaschke et al., 2018; Russell et al., 1987). In the near-Earth space, the global distribution of the magnetic cavities is given in Yao et al. (2021).

Magnetic cavities have been widely believed to be generated via the mirror (Winterhalter et al., 1994) or electron-mirror instabilities (Hellinger and Stverak, 2018; Yao, Shi, Yao, Guo, et al., 2019), as is supported by the observations with particle fluxes concentrated in the direction perpendicular to the magnetic field (Gershman et al., 2016; Winterhalter et al., 1994). Most of the magnetic cavities have been found to be associated with hot particle populations concentrated in pitch angles near 90°, which contribute to the ring-shaped azimuthal current consistent with the reduced magnetic field strength (Haynes et al., 2015; Yao et al., 2017; Zhang et al., 2017). In some other events, donut-shaped particle pitch angle distributions (PADs) have been identified (Yao et al., 2018; Ahmadi et al., 2018), which according to Li, Zhou, et al. (2020) could originate from the deepening and/or shrinking processes of the magnetic cavities (Liu et al., 2019b, 2020; Yao, Hamrin, et al., 2020). It is the anisotropic particle distributions that provide the free energy for excitation of various plasma waves often observed in magnetic cavities (Ahmadi et al., 2018; Huang et al., 2018, 2020; Yao, Shi, Yao, Li, et al., 2019). In recent years, the availability of high-resolution observations from the Magnetospheric Multi-Scale (MMS) constellation (Burch et al., 2016) enables identification of electron-scale (with the radius of several electron thermal gyroradii ρ_e) magnetic cavities (Gershman et al., 2016; Huang et al., 2017; Yao et al., 2017). In certain cases, these electron-scale cavities are embedded within ion-scale magnetic cavities (Liu et al., 2019a), which supports the scenario that magnetic cavities play important roles in the energy exchange and cascade of turbulent plasmas (Huang et al., 2017; Sahraoui et al., 2006).

On the other hand, kinetic simulations have shown that electron-scale magnetic cavities are stationary in the ion fluid rest frame and quasi-stable for at least hundreds of electron gyroperiod (Haynes et al., 2015). A consequent hypothesis is that magnetic cavities can be described by kinetic equilibrium models satisfying the Vlasov-Maxwell equations in cylindrical coordinates (Li et al., 2020a; Shustov et al., 2016). In the Shustov et al. (2016) model, the particle distributions are constructed as functions of two invariants of motion, including the particle energy and the canonical angular momentum in the azimuthal direction, which are then substituted into the Maxwell equations to achieve the self-consistent solution of the particle and electromagnetic field profiles. Based on the same framework, Li et al. (2020a) takes into account the electron magnetic moment as an additional invariant of motion in the kinetic model. The reconstructed profiles show good agreement with the observations from multiple MMS spacecraft, which demonstrates the existence of equilibrium-state, nested electron- and ion-scale cavities in the turbulent space plasma environment.

Despite the success in reproducing the observations in specific events, the kinetic models described above have a limited applicability in that the particle distributions are always symmetric in the background magnetic field direction. In other words, the electric current in the modeled magnetic cavities cannot have an axial component, which makes it impossible to reproduce the MMS observations of helical magnetic cavities with nonzero magnetic field components in both axial and azimuthal directions (Huang et al., 2017). In this paper, we introduce another invariant of motion, the canonical axial momentum, into the Li et al. (2020a) model to enable an axial velocity shift in the electron distributions. We will show that the modified model can reproduce the helical magnetic field lines, together with other observational characteristics in Huang et al. (2017).

2. Observations

In this section, we provide a brief revisit to the observations of a helical magnetic cavity (Huang et al., 2017). This specific cavity was observed in the magnetosheath by the MMS constellation on 08:48:47, October 25, 2015, during which the four MMS spacecraft were separated from one another by less than 20 km. The MMS observational data utilized include the electron three-dimensional velocity distributions from fast plasma investigation (FPI) instruments (Pollock et al., 2016) and the electromagnetic field measurements from FIELDS instrument suite (Torbert et al., 2016).

The magnetic field depression was observed by MMS1, MMS2, and MMS3 (with the neighboring MMS4 hardly observing any magnetic field perturbations), which is consistent with the inferred cavity radius of 15 km (Huang et al., 2017) in the plane perpendicular to the background magnetic field. Figure 1 provides the observations from MMS1 (upper left panels) and MMS3 (upper right panels) within a 0.3-s time interval starting from 08:48:46.9 UT. The observations from MMS2 are not shown here, since it only grazed the cavity edge as indicated by the weak (~1 nT) magnetic field perturbations. Figure 1a1–1a3 show the MMS1 observations of the depressed magnetic field strength, the enhanced plasma density, and the enhanced electron temperature in the perpendicular direction, respectively, which are the characteristic features of the

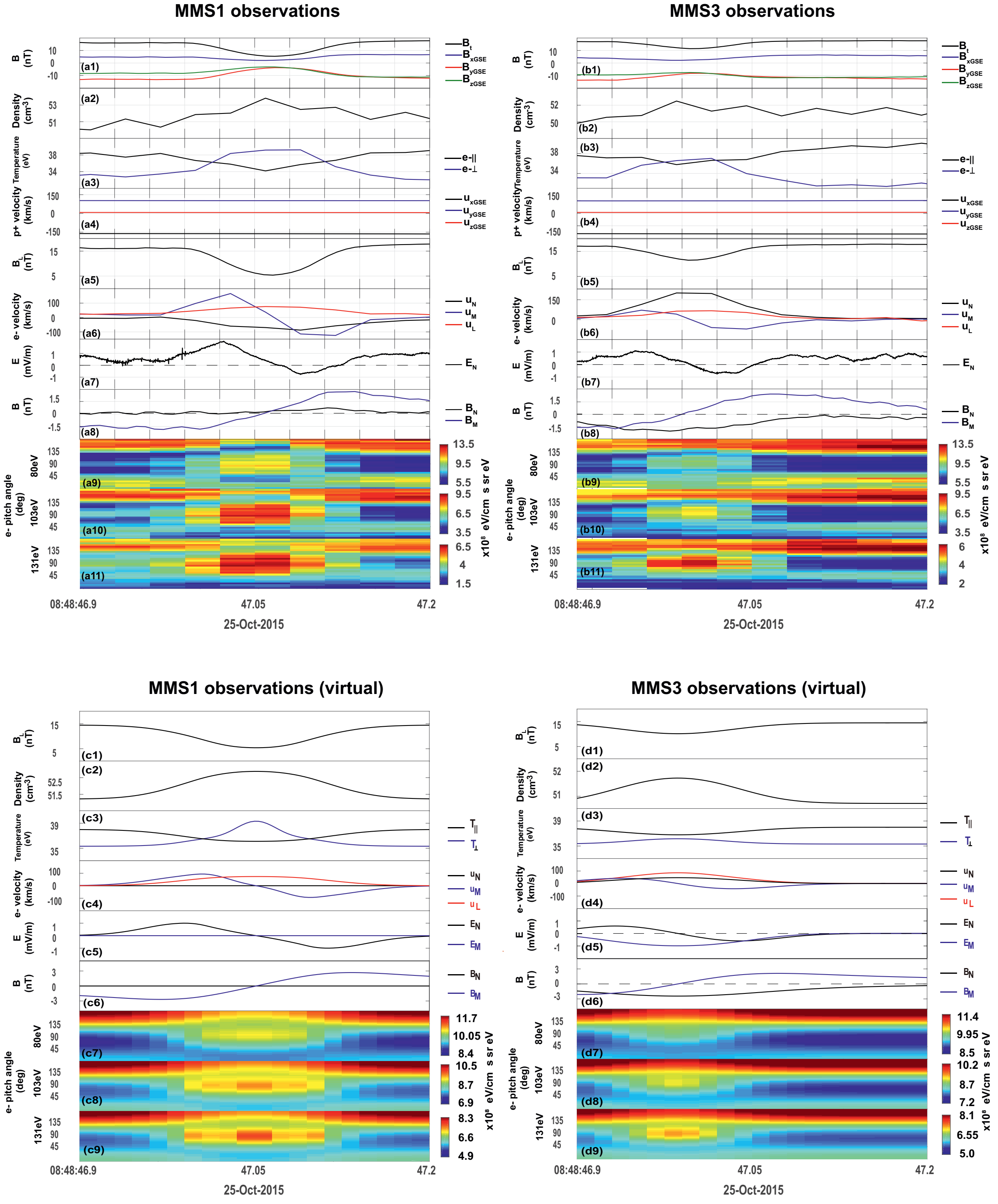
MMS1 observations
MMS3 observations
B (nT)
Bt
BxGSE
ByGSE
BzGSE
(a1)
(a2)
(a3)
(a4)
(a5)
(a6)
(a7)
(a8)
(a9)
(a10)
(a11)
(b1)
(b2)
(b3)
(b4)
(b5)
(b6)
(b7)
(b8)
(b9)
(b10)
(b11)
Density (cm-3)
Temperature (eV)
e-||
e-⊥
p+ velocity (km/s)
uxGSE
uyGSE
uzGSE
BL (nT)
e- velocity (km/s)
uN
uM
uL
E (mV/m)
EN
BN
BM
e- pitch angle (deg)
80eV
103eV
131eV
x10^8 eV/cm s sr eV
08:48:46.9
47.05
47.2
25-Oct-2015
MMS1 observations (virtual)
MMS3 observations (virtual)
(c1)
(c2)
(c3)
(c4)
(c5)
(c6)
(c7)
(c8)
(c9)
(d1)
(d2)
(d3)
(d4)
(d5)
(d6)
(d7)
(d8)
(d9)
T||
T⊥
EM

magnetic cavity. The ion bulk velocity, shown in Figure 1a4, hardly changed during this time interval indicating that the electron-scale magnetic cavity was quasi-stationary in the rest frame of the ion fluid (Haynes et al., 2015). Based on these observations, a local LMN coordinate system is defined and used throughout the paper, in which the L axis (0.33, −0.75, −0.58, GSE) is along the average magnetic field direction, the N (0.86, −0.01, 0.51, GSE) axis is opposite to the ion bulk velocity projected into the perpendicular plane, and the M (0.39, 0.66, −0.64, GSE) axis completes the orthogonal triad.

Figure 1a5 shows the B_L component, which experiences a negative excursion from 15 to 5 nT in agreement with the field strength variations shown in Figure 1a1. Figure 1a6 shows the electron bulk velocity in the reference frame of the ion fluid (or equivalently, the rest frame of the magnetic cavity), which exhibits bipolar variations in the M direction indicating the azimuthal electron flows in the cavity rest frame. We also carry out a Lorentz transformation to present in Figure 1a7 the electric field in the cavity rest frame, which shows bipolar variations in the N direction indicating the presence of radially inward electric field (Goodrich et al., 2016a, 2016b). Figure 1a9–1a11 show the suprathermal electron pitch-angle distributions in the spacecraft rest frame within the energy channels of 80 , 103, and 131 eV, respectively (the thermal electron distributions are not shown since they hardly varied across the cavity and contributed only slightly to the current and pressure variations). In each energy channel, the perpendicular electron fluxes were always higher than in the parallel direction near the cavity center, and lower outside the cavity. The location-dependent anisotropy can be also seen in Figure 1a3, with higher and lower perpendicular temperature than parallel temperature inside and outside the cavity, respectively. These characteristics are all consistent with previous observations and modeling results in Li et al. (2020a).

In this event, however, a new feature appears in that the magnetic field B_M component exhibits bipolar variations (see Figure 1a8), which indicates the presence of azimuthal magnetic field in the clockwise direction and consequently, the helical magnetic field lines within the cavity. This configuration requires an electric current in the anti-parallel direction, which may appear inconsistent with the electron pitch-angle distributions in Figure 1a9–1a11 showing higher fluxes in the anti-parallel than in the parallel direction. This is because the electron distributions were measured in the spacecraft rest frame. After a transformation into the ion fluid rest frame, the electron bulk velocity was indeed in the parallel direction (see Figure 1a6) to carry the anti-parallel current.

The MMS3 observations (shown in the upper right panels of Figure 1) exhibit similar signatures to the MMS1 observations, including the depressed magnetic field (Figure 1b1 and 1b5), the enhanced plasma density (Figure 1b2) and perpendicular pressure (Figure 1b3), the bipolar variations of the electron velocity u_M (Figure 1b6), electric field E_N components (Figure 1b7), the magnetic field B_M (Figure 1b8), and the anisotropic electron distributions (Figure 1b9–1b11). The major difference between them is that MMS3 experienced a less significant B_L reduction to 12 nT (rather than 5 nT as observed by MMS1) within a shorter time interval (see Figure 1b5), which can be attributed to the different paths the two MMS spacecraft moved across the magnetic cavity. According to Huang et al. (2017), MMS1 traversed the cavity center whereas MMS3 only encountered the outer portion of the cavity. We also note that the B_N field showed a unipolar, negative profile in MMS3 observations (Figure 1b8), although it was very close to zero in MMS1 observations (Figure 1a8). This feature is also consistent with their different traversal paths across the cavity with helical magnetic field lines.

Figure 1. MMS1 (left panels) and MMS3 (right panels) in-situ observations (upper panels) of the helical magnetic cavity on October 25, 2015, together with the corresponding virtual observations (lower panels) of the modeled magnetic cavity. MMS1 observations of the (a1) magnetic field in the GSE coordinates (a2) electron number density (a3) electron temperatures in the perpendicular (blue) and parallel (black) directions (a4) ion bulk velocity in the GSE coordinates (a5) magnetic field B_L component in the LMN coordinates (a6) electron bulk velocity in the rest frame of the ion fluid, also given in the LMN coordinates (a7) electric field E_N component, after a Lorentz transformation into the ion rest frame (a8) magnetic field B_N and B_M component (a9-a11) electron pitch-angle distributions in the 80 , 103, and 131 eV energy channels (b1-b11) MMS3 observations in the same format as in Panels a1-a11. Virtual observations at MMS1 location of the (c1) magnetic field B_L component (c2) electron number density (c3) electron temperatures in the perpendicular (blue) and parallel (black) directions (c4) electron bulk velocity in the LMN coordinates (c5) electric field E_N and E_M components (c6) magnetic field B_N and B_M components (c7-c9) pitch-angle distributions of the 80 eV, 103 and 131 eV electrons in the spacecraft rest frame (d1-d9) Virtual observations at MMS3 in the same format as Panels c1-c9. MMS, magnetospheric multi-scale.

3. Model Development

Before we develop the model to reproduce the observations, we next review the kinetic, equilibrium model of magnetic cavities developed in Li et al. (2020a). The Li et al. (2020a) model is constructed in a cylindrical coordinate system (ρ, φ, ζ), in which ρ, φ, and ζ are the radial, azimuthal, and axial coordinates. In this model, the magnetic vector potential $\boldsymbol{A} = A_\varphi(\rho)\boldsymbol{e_\varphi}$ and the electric scalar potential $\phi = \phi(\rho)$ are both independent of φ and ζ, indicating that the magnetic field is in the axial direction and the electric field is in the radial direction. The Hamiltonian of a charged particle, or equivalently its total energy in the electromagnetic field can thus be given by

$$H_\alpha = \frac{1}{2m_\alpha}\left(\boldsymbol{P} - q_\alpha \boldsymbol{A}\right)^2 + q_\alpha \phi, \tag{1}$$

where $\alpha = e{,}i$ represents the particle species (electrons or protons), and $\boldsymbol{P}$ is the canonical momentum in cylindrical coordinates. Note that the azimuthal component of $\boldsymbol{P}$, the canonical angular momentum P_φ given by

$$P_{\varphi\alpha} = \rho\left(M_\alpha v_\varphi + q_\alpha A_\varphi\right), \tag{2}$$

is also an invariant of motion since H_α is independent of φ. In this system, there is another adiabatic invariant of motion, the magnetic moment of an electron (but not a proton due to its larger gyroradius than a kinetic-scale cavity) given by

$$\mu_e = \frac{M_e\left|\boldsymbol{v}_\perp - \boldsymbol{v}_D\right|^2}{2B_\zeta}, \tag{3}$$

where v_D represents the electron's drift velocity. To satisfy the equilibrium-state Vlasov equation, these invariants of motion are used to construct the particle distributions,

$$f_e = \delta N_e\left(\frac{M_e}{2\pi\theta_{e,0}}\right)^{\frac{3}{2}}\exp\left(-\frac{H_e + b_{e,0}\mu_e}{\theta_{e,0}}\right) + \left(1-\delta\right)N_e\left(\frac{M_e}{2\pi\theta_{e,1}}\right)^{\frac{3}{2}}\exp\left(-\frac{H_e - \Omega_e P_{\varphi e} + b_{e,1}\mu_e}{\theta_{e,1}}\right), \tag{4}$$

$$f_i = \delta N_i\left(\frac{M_i}{2\pi\theta_{i,0}}\right)^{\frac{3}{2}}\exp\left(-\frac{H_i}{\theta_{i,0}}\right) + \left(1-\delta\right)N_i\left(\frac{M_i}{2\pi\theta_{i,1}}\right)^{\frac{3}{2}}\exp\left(-\frac{H_i - \Omega_i P_{\varphi i}}{\theta_{i,1}}\right), \tag{5}$$

in which each particle species has a background population and a current-carrying population denoted by subscripts 0 and 1, respectively. Only the latter population depends on $P_{\varphi\alpha}$, which contributes to the azimuthal current required for the magnetic cavity formation. Here, δ represents the density share of the background population at the cavity center, N_α and θ_α are the nominal plasma density and temperature, and Ω_α represents the angular bulk velocity of the current-carrying population in the azimuthal direction. In this model, the electron temperature anisotropy is determined by the $b_{e,0}$ and $b_{e,1}$ indices, which is made possible by the fact that the μ_e invariant depends on the electron kinetic energy in the perpendicular but not parallel directions. These distribution functions are then integrated to obtain the number density n_α and the current density j_α, which in turn are substituted into the Ampere's law (Equation 6) and the quasi-neutrality condition (Equation 7),

$$\frac{\partial}{\partial\rho}\left[\frac{1}{\rho}\frac{\partial}{\partial\rho}\left(\rho A_\varphi\right)\right] = -\mu_0\left(j_{e,\varphi} + j_{i,\varphi}\right), \tag{6}$$

$$n_e = n_i. \tag{7}$$

The solution to these equations, given the boundary value of B_ζ at $\rho = 0$, provides the self-consistent profiles of the electromagnetic field and particle phase space densities.

We point out that the three invariants of motion, given in Equations 1–3, are either independent of, or even functions of the particle's axial velocity v_ζ. Therefore, the Li et al. (2020a) model cannot accommodate the axial current required for the helical magnetic cavity observed in Figure 1. To introduce the azimuthal magnetic field B_φ into the model, the magnetic vector potential $\boldsymbol{A}$ must have both azimuthal and axial components, that is, $\boldsymbol{A} = A_\varphi(\rho)\boldsymbol{e}_\varphi + A_\zeta(\rho)\boldsymbol{e}_\zeta$. Given that the Hamiltonian H is independent on ζ, the electron's canonical momentum in the axial direction,

$$P_{\zeta e} = M_e v_\zeta + q_e A_\zeta, \tag{8}$$

can be treated as another invariant of motion. Therefore, we revise the Li et al. (2020a) model by incorporating $P_{\zeta e}$ into the electron distribution functions, to have Equation 4 replaced by

$$f_e = \delta N_e \left(\frac{M_e}{2\pi\theta_{e,0}}\right)^{\frac{3}{2}} exp\left(-\frac{H_e + b_{e,0}\mu_e}{\theta_{e,0}}\right) + \left(1-\delta\right) N_e \left(\frac{M_e}{2\pi\theta_{e,1}}\right)^{\frac{3}{2}} exp\left(-\frac{H_e - \Omega_e P_{\varphi e} + b_{e,1}\mu_e + u_{e,1}P_{\zeta e}}{\theta_{e,1}}\right), \tag{9}$$

and we keep the proton distributions (Equation 5) unchanged in the model. The linear combination of the four invariants of motion in the second term indicates that the current-carrying electron population can be approximately described by bi-Maxwellian velocity distributions shifted in the azimuthal and axial directions, with the axial shift determined by the newly introduced parameter $u_{e,1}$. It is this axial bulk velocity that contributes to the azimuthal magnetic field B_φ in the helical magnetic cavity.

We next follow Li et al. (2020a) to integrate the particle distributions, and substitute the resulting current and number densities into the Ampere's law and the quasi-neutrality equations, respectively. In this new model, the presence of A_ζ indicates that the Ampere's law has another component in addition to Equation 6, that is,

$$\frac{1}{\rho}\left[\frac{\partial}{\partial\rho}\left(\rho\frac{\partial A_\zeta}{\partial\rho}\right)\right] = -\mu_0 j_{e,\zeta}, \tag{10}$$

and the solution provides the self-consistent plasma and electromagnetic field profiles in the helical magnetic cavity

4. Model Results and Comparison with Observations

In this section, we utilize the newly developed model to reconstruct the helical magnetic cavity observed in Figure 1. The model parameters, adopted to match the MMS1 observations (with the assumption that MMS1 moved across the magnetic cavity center, see discussions in the observations section), are as follows: $\delta = 0.8$, $N_e = 57.5\ \text{cm}^{-3}$, $\Omega_e = 61.5\ \text{s}^{-1}$, $\Omega_i = 0\ \text{s}^{-1}$,$u_{e,1} = 250$ km/s, $\theta_{e,0} = 38$ eV, $\theta_{e,1} = 31.5$ eV, $\theta_{i,0} = 310$ eV, $\theta_{i,1} = 310$ eV, $b_{e,0} = 1.1$ nT, and $b_{e,1} = -2.9$ nT. Figure 2a shows the 3-dimensional configuration of the modeled cavity, in which the magnetic field lines are clearly helical. The perpendicular cross-section of the cavity is given in Figure 2b, with the arrows and colors representing the B_φ and B_ζ distributions, respectively.

The profiles of the electromagnetic field and plasma moments as functions of the radial distance ρ are given in Figures 2c–2h. An interesting feature of the cavity is that the electron bulk velocity u_φ in the azimuthal direction increases from zero at the cavity center to its peak at $\rho \sim 6$ km and gradually decreases to approach zero at $\rho \to \infty$ (see Figure 2f). The electron bulk velocity u_ζ in the axial direction, on the other hand, peaks at the cavity center and decreases with ρ. This is because the density of the current-carrying electron population (the second term in Equation 9) decreases with ρ, which largely originates from the A_φ-dependence of the electron phase space densities (since P_φ depends on A_φ, see Equation 2). Therefore, even if this population has an increasing azimuthal bulk velocity with ρ (due to the constant angular velocity Ω_e), its decreasing proportion in total plasma density can revoke this effect to produce the single-peaked u_φ profile in Figure 2f. One may also find from Equation 9 that the axial velocity of the current-carrying electron population is constant, which indicates that u_ζ would also decrease with ρ at the same rate as the density

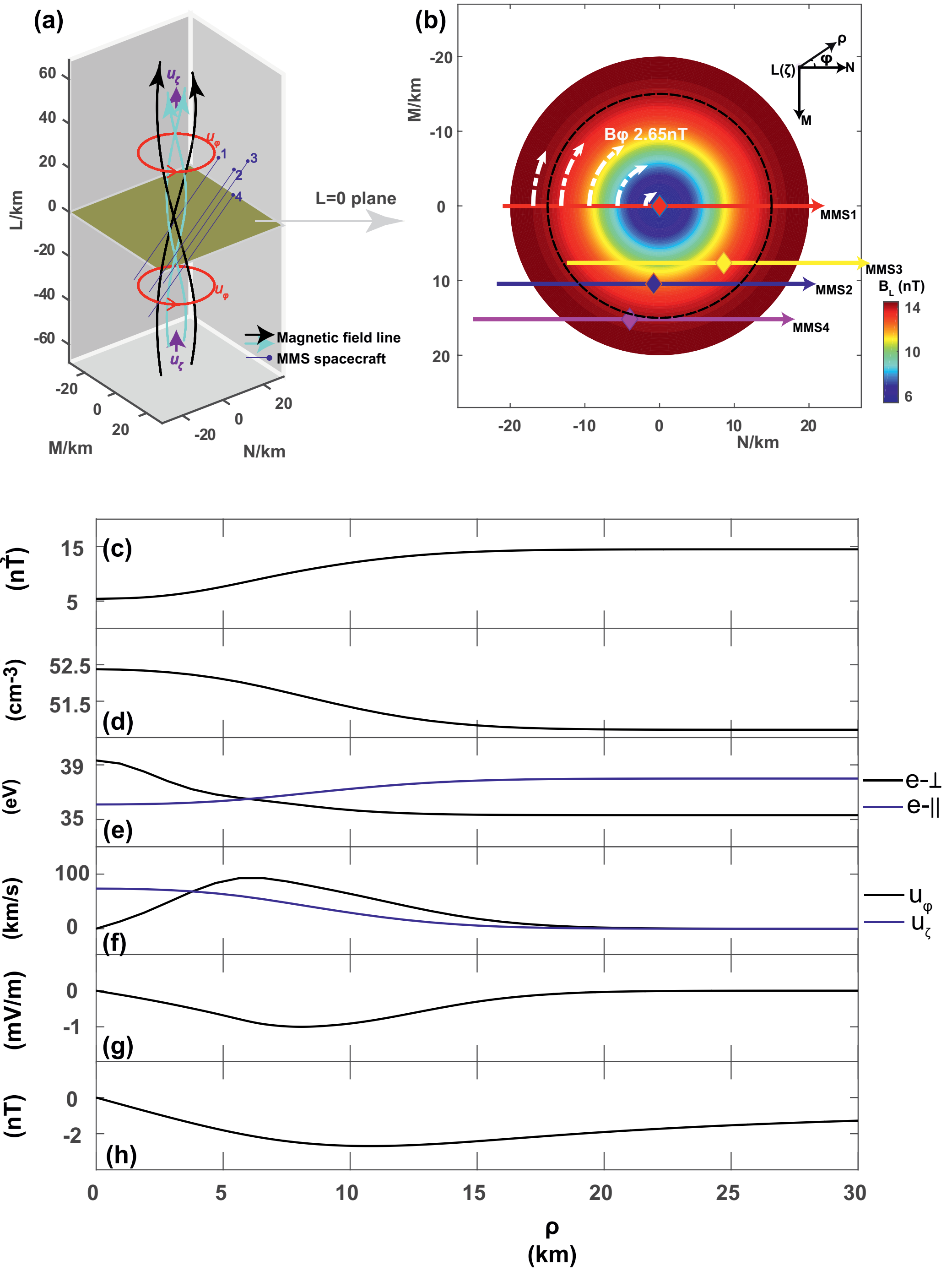

Figure 2. Profiles of the magnetic cavity model. (a) The 3-dimensional illustration of the helical magnetic field lines within the cavity, with the red and purple arrows indicating the electron bulk velocity in the azimuthal and axial directions, respectively. The white lines represent the oblique trajectories of the four MMS spacecraft in the cavity rest frame. (b) The cross section of the magnetic cavity in the MN plane. The color and the white arrows represent the magnetic field B_ζ and B_φ components, respectively. The bottom panels are the magnetic cavity profiles as functions of radial distance to the center, showing (c) the magnetic field B_ζ component, (d) the number density, (e) the electron parallel and perpendicular temperatures, (f) the electron bulk velocity, (g) the radial electric field, and (h) the magnetic field B_φ component. MMS, magnetospheric multi-scale.

of the current-carrying population. Moreover, since the background and the current-carrying populations have different temperatures in both perpendicular and parallel directions, the variations of their density proportions with ρ also lead to the temperature and anisotropy variations shown in Figure 2e.

In Figures 2a and 2b, we also show the trajectories of the MMS constellation across the modeled cavity, with their moving velocity in the rest frame of the cavity being opposite to the observed ion bulk velocity, that is, 134 km/s and 136 km/s along the L and N directions, respectively. As discussed before, the MMS1 trajectory traverses the cavity center, whereas MMS3 only reaches the outer portion of the magnetic cavity. Based on these trajectories, we are now able to present in the lower panels of Figure 1 the virtual observations of the modeled cavity as functions of time at the MMS1 and MMS3 locations. These virtual observations, presented in the same format as in the upper panels for real observations (except that the virtual observations of the ion bulk velocity are not shown since they are constant in the model), can be directly compared to the MMS observations.

More specifically, Figure 1c1–1c3 show the characteristic signatures of depressed B_L field, enhanced plasma density, and enhanced electron pressure in the perpendicular direction. The electron parallel pressure, also given in Figure 1c3, shows a negative excursion within the cavity in good agreement with the MMS1 observations (see Figure 1a3). The electron bulk velocities in Figure 1c4 are characterized by the bipolar u_M and unipolar u_L variations, and the modeled electric field in Figure 1c5 shows bipolar E_N variations, both of which are also consistent with the corresponding measurements in Figure 1a6 and 1a7. More importantly, the model reproduces the helical magnetic field lines characterized by the bipolar B_M variations (compare Figure 1a8 and 1c6).

Figure 1c7–1c9 present the modeled electron pitch-angle distributions in the same energy channels as in Figure 1a9–1a11. They show excellent agreement with the observations in that the electrons are 90°-concentrated near the cavity center, whereas their axial fluxes are higher in the outer portion of the cavity. Moreover, the modeled electron distributions reproduce the observations in that electron fluxes in the anti-parallel direction are much higher than in the parallel direction, which is especially significant at the outer portion of the cavity where the background population (the first term in Equation 9) dominates. This specific feature, as discussed before, originates from the coordinate transformation between the rest frames of the spacecraft and the magnetic cavity. One may think that their relative motion, 134 km/s in the L direction and equivalent to the speed of a 0.05-eV electron, could not cause any discernible difference in the energy range of interest at ∼100 eV. These arguments are not true, since the exponential form of the Maxwellian-type distributions (see Equation 9) indicates that a minor shift in the electron velocity would lead to a significant difference in phase space densities. If we consider the background electrons at any given energy W, the ratio between the electron fluxes in the anti-parallel and parallel directions would be

$$\frac{f_{anti}}{f_{para}} = \exp\left[\frac{M_e\left(v_s + \left|v_\zeta\right|\right)^2 - M_e\left(v_s - \left|v_\zeta\right|\right)^2}{2\theta_{e,0}}\right] = \exp\left(\frac{2M_e v_s \left|v_\zeta\right|}{\theta_{e,0}}\right) \tag{11}$$

where $v_\zeta = (2\,W/M_e)^{1/2}$ is the velocity of the parallel-moving electron, and v_s represents the axial component of the spacecraft moving velocity (134 km/s in this event). Therefore, the ratio becomes larger for electrons with higher energies, which is approximately 1.3 for 100-eV electrons to account for the observations of asymmetric electron distributions despite the slow spacecraft velocity in this event.

Before we turn to the virtual observations at MMS3, we should note that our model could not reproduce the unipolar u_N variations observed in Figure 1a6. In fact, the modeled electron distributions in Equation 9 are even functions of the electron radial velocity v_ρ, which indicates that the radial component of the electron bulk velocity must be zero. This discrepancy could be resolved by a minor deviation of the MMS1 trajectory from the cavity center (so that the N and the ρ directions would not overlap); however, the deviation would also correspond to nonzero B_N variations that were not observed in Figure 1a8. A possible explanation is the different spatial scales of the axial and azimuthal current profiles, which can be achieved by varying the model parameters (especially Ω_e, $u_{e,1}$, and $\theta_{e,1}$) or developing more sophisticated models based on different combinations of the invariants of motion. Here, we determine that this inconsistency is relatively minor, and we make no attempt to fully reconcile it in this paper.

Finally, we point out that the virtual observations at MMS3 (lower right panels of Figure 1) are consistent with real observations (upper right panels of Figure 1), even if the model parameters are determined based on the match with MMS1 but not MMS3 data. The mostly consistent predictions and observations, therefore, validate the model of helical magnetic cavities and supports the scenario that quasi-equilibrium, electron-scale magnetic cavities can be formed to travel with the ion flows during the turbulent evolution of space plasmas.

5. Conclusions

In this paper, we revisit the MMS observations of an electron-scale magnetic cavity previously reported by Huang et al. (2017). The existence of helical magnetic field lines in the cavity indicates that it cannot be reproduced by any earlier models of kinetic magnetic cavities (Li et al., 2020a; Shustov et al., 2016). To accommodate the helical field lines, we incorporate an additional invariant of electron motion, the canonical axial momentum, into the Li et al. (2020a) model to resolve the self-consistent electromagnetic field and particle distributions within the magnetic cavity. In this model, the involvement of the new invariant enables the current-carrying electrons to flow in the axial direction, which in turn produce the azimuthal magnetic field component required for the helical structure. Making an analogy to classical plasma structures, a magnetic cavity with the azimuthal current density can be considered as the theta-pinch (Li et al., 2020a; Shustov et al., 2016), whereas the presented model of the cavity with axial and azimuthal currents resembles the theta-z-pinch (similar kinetic equilibria are considered in respect to flux-ropes, see Vinogradov et al., 2016; Allanson et al., 2016).

We next utilize this new model to reconstruct the helical magnetic cavity, with the model parameters adopted to match the MMS1 observations in both the electromagnetic field and particle distributions. Based on the same parameters, the model also predicts the signatures observable at the neighboring MMS3 spacecraft. The consistency between the predictions and the MMS3 observational data supports the validity of the new model in describing the equilibrium-state, helical magnetic cavities. In the future, we plan to utilize this model as the initial condition, to explore the kinetic evolution and instabilities associated with magnetic cavities.

Data Availability Statement

We are grateful to the MMS team for providing the high-quality observational data utilized in this study, which are available from the MMS science data center (https://lasp.colorado.edu/mms/sdc/public/). The model codes are available from the Zenodo repository (https://doi.org/10.5281/zenodo.4497596).

Acknowledgments
This study was supported by NSFC grants 41774168 and 41421003.

References

Ahmadi, N., Wilder, F. D., Ergun, R. E., Argall, M., Usanova, M. E., Breuillard, H., et al. (2018). Generation of electron whistler waves at the mirror mode magnetic holes: MMS observations and PIC simulation. *Journal of Geophysical Research: Space Physics*, *123*, 6383–6393. https://doi.org/10.1029/2018JA025452

Allanson, O., Wilson, F., & Neukirch, T. (2016). Neutral and non-neutral collisionless plasma equilibria for twisted flux tubes: The Gold-Hoyle model in a background field. *Physics of Plasmas*, *23*(9), 092106.

Balikhin, M. A., Sibeck, D. G., Runov, A., & Walker, S. N. (2012). Magnetic holes in the vicinity of dipolarization fronts: Mirror or tearing structures? *Journal of Geophysical Research: Space Physics*, *117*, A08229. https://doi.org/10.1029/2012JA017552

Burch, J. L., Moore, T. E., Torbert, R. B., & Giles, B. L. (2016). Magnetospheric multiscale overview and science objectives. *Space Science Reviews*, *199*(1–4), 5–21.

Burlaga, L. F., Ness, N. F., & Acũna, M. H. (2006). Trains of magnetic holes and magnetic humps in the heliosheath. *Geophysical Research Letters*, *33*, L21106. https://doi.org/10.1029/2006GL027276

Cattaneo, M. B. B., C. Basile, G. Moreno, and J. D. Richardson (1998), Evolution of mirror structures in the magnetosheath of Saturn from the bow shock to the magnetopause, *Journal of Geophysical Research*, *103*, 11961–11972. https://doi.org/10.1029/97JA03683

Ge, Y. S., McFadden, J. P., Raeder, J., Angelopoulos, V., Larson, D., & Constantinescu, O. D. (2011). Case studies of mirror-mode structures observed by THEMIS in the near-Earth tail during substorms. *Journal of Geophysical Research*, *116*, A01209. https://doi.org/10.1029/2010JA015546

Gershman, D. J., Dorelli, J. C., Viñas, A. F., Avanov, L. A., Gliese, U., Barrie, A. C., et al. (2016). Electron dynamics in a subproton-gyroscale magnetic hole. *Geophysical Research Letters*, *43*, 4112. https://doi.org/10.1002/2016GL068545

Goodrich, K. A., Ergun, R. E., & Stawarz, J. E. (2016b). Electric fields associated with small-scale magnetic holes in the plasma sheet: Evidence for electron currents. *Geophysical Research Letters*, *43*, 6044–6050. https://doi.org/10.1002/2016GL069601

Goodrich, K. A., Ergun, R. E., Wilder, F. D., Burch, J., Torbert, R., Khotyaintsev, Y., et al. (2016a). MMS Multipoint electric field observations of small-scale magnetic holes. *Geophysical Research Letters*, *43*, 5953–5959. https://doi.org/10.1002/2016GL069157

Haynes, C. T., Burgess, D., Camporeale, E., & Sundberg, T. (2015). Electron vortex magnetic cavities: A nonlinear coherent plasma structure. *Physics of Plasmas*, *22*, 012309.

Hellinger, P., & Štverák, Š. (2018). Electron mirror instability: Particle-in-cell simulations. *Journal of Plasma Physics*, *84*(4), 905840402. https://doi.org/10.1017/S0022377818000703

Huang, S. Y, Sahraoui, F., Yuan, Z. G., He, J. S., Zhao, J. S., Le Contel, O., et al. (2017). Magnetospheric multi-scale observations of electron vortex magnetic hole in the turbulent magnetosheath plasma. *The Astrophysical Journal Letters*, *836*. https://doi.org/10.3847/2041-8213/aa5f50

Huang, S. Y., Sahraoui, F., Yuan, Z. G., Le Contel, O., Breuillard, H., He, J. S., et al. (2018). Observations of whistler waves correlated with electron-scale coherent structures in the magnetosheath turbulent plasma. *The Astrophysical Journal*, *861*, 29. https://doi.org/10.3847/1538-4357/aac831

Huang, S. Y., Xu, S. B., He, L. H., Jiang, K., Yuan, Z. G., Deng, X. H., et al. (2020). Excitation of whistler waves through the bidirectional field-aligned electron beams with electron temperature anisotropy: MMS observations. *Geophysical Research Letters*, *47*, e2020GL087515. https://doi.org/10.1029/2020GL087515

Joy, S. P., Kivelson, M. G., Walker, R. J., Khurana, K. K., Russell, C. T., & Paterson, W. R. (2006). Mirror-mode structures in the Jovian magnetosheath. *Journal of Geophysical Research*, *111*, A12212. https://doi.org/10.1029/2006JA011985

Li, J., Zhou, X., Zong, Q., Yang, F., Fu, S., Yao, S., et al. (2020b). On the Origin of Donut-shaped Electron Distributions within Magnetic Cavities. *Geophysical Research Letters*, *47*, e2020GL091613. https://doi.org/10.1029/2020GL091613

Li, J.-H., Yang, F., Zhou, X. Z., Zong, Q. G., Artemyev, A. V., Rankin, R., et al. (2020a). Self-consistent kinetic model of nested electron- and ion-scale magnetic cavities in space plasmas. *Nature Communications*, *11*, 5616. https://doi.org/10.1038/s41467-020-19442-0

Liu, H., Zong, Q.-G., Zhang, H., Sun, W. J., Zhou, X.-Z., Gershman, D. J., et al. (2019b). The geometry of an electron scale magnetic cavity in the plasma sheet. *Geophysical Research Letters*, *46*, 9308–9317. https://doi.org/10.1029/2019GL083569

Liu, H., Zong, Q. G., Zhang, H., Xiao, C. J., Shi, Q. Q., Yao, S. T., et al. (2019a). MMS observations of electron scale magnetic cavity embedded in proton scale magnetic cavity. *Nature Communications*, *10*, 1040. https://doi.org/10.1038/s41467-019-08971-y

Liu, J., Yao, S. T., Shi, Q. Q., Wang, X. G., Zong, Q. G., Feng, Y. Y., et al. (2020). Electron energization and energy dissipation in microscale electromagnetic environments. *The Astrophysical Journal Letters*, *889*, 2. https://doi.org/10.3847/2041-8213/abab92

Plaschke, F., Karlsson, T., Goetz, C., Moestl, C., Richter, I., Volwerk, M., et al. (2018). First observations of magnetic holes deep within the coma of a comet. *Astronomy & Astrophysics*, *618*, A114. https://doi.org/10.1051/0004-6361/201833300

Pollock, C., Moore, T., Jacques, A., Burch, J., Gliese, U., Saito, Y., et al. (2016). Fast plasma investigation for magnetospheric multi-scale. *Space Science Reviews*, *199*, 331–406. https://doi.org/10.1007/s11214-016-0245-4

Russell, C. T., Jian, L. K., Luhmann, J. G., Zhang, T. L., Neubauer, F. M., Skoug, R. M., et al. (2008). Mirror mode waves: Messengers from the coronal heating region. *Geophysical Research Letters*, *35*(15). https://doi.org/10.1029/2008GL034096

Russell, C. T., Riedler, W., Schwingenschuh, K., & Yeroshenko, Y. (1987). Mirror instability in the magnetosphere of comet Halley. *Geophysical Research Letters*, *14*, 644. https://doi.org/10.1029/GL014i006p00644

Sahraoui, F., Belmont, G., Rezeau, L., Cornilleau-Wehrlin, N., Pinçon, J. L., & Balogh, A. (2006). Anisotropic turbulent spectra in the terrestrial magnetosheath as seen by the Cluster spacecraft. *Physical Review Letters*, *96*, 075002. https://doi.org/10.1103/PhysRevLett.96.075002

Shustov, P., Nishimura, Y., Artemyev, A. V., Zhang, X.-J., Angelopoulos, V., & Petrukovich, A. A. (2020). In-situ and optical observations of sub-ion magnetic holes. *Journal of Atmospheric and Solar-Terrestrial Physics*. https://doi.org/10.1016/j.jastp.2020.105365

Shustov, P., Zhang, X.-J., Pritchett, P., Artemyev, A. V., Angelopoulos, V., Yushkov, E., et al. (2019). Statistical properties of sub-ion magnetic holes in the dipolarized magnetotail: Formation, structure, and dynamics. *Journal of Geophysical Research: Space Physics*, *124*, 342. https://doi.org/10.1029/2018JA025852

Shustov, P. I., Artemyev, A. V., Vasko, I. Y., & Yushkov, E. V. (2016). Kinetic models of sub-ion cylindrical magnetic hole. *Physics of Plasmas*, *23*, 122903. https://doi.org/10.1063/1.4972093

Sun, W. J., Shi, Q. Q., Fu, S. Y., Pu, Z. Y., Dunlop, M. W., Walsh, A. P., et al. (2012). Cluster and TC-1 observation of magnetic holes in the plasma sheet. *Annals of Geophysics*, *30*, 583–595. https://doi.org/10.5194/angeo-30-583-2012

Sundberg, T., Burgess, D., & Haynes, C. T. (2015). Properties and origin of subproton-scale magnetic cavities in the terrestrial plasma sheet. *Journal of Geophysical Research - A: Space Physics*, *120*, 2600–2615.

Torbert, R. B., Russell, C. T., Magnes, W., Ergun, R. E., Lindqvist, P. A., LeContel, O., et al. (2016). The FIELDS instrument suite on MMS: Scientific objectives, measurements, and data products. *Space Science Reviews*, *199*, 105–135. https://doi.org/10.1007/s11214-014-0109-8

Tsurutani, B. T., Lakhina, G. S., Verkhoglyadova, O. P., Echer, E., Guarnieri, F. L., Narita, Y., et al. (2011). magnetosheath and heliosheath mirror mode structures, interplanetary magnetic decreases, and linear magnetic decreases: Differences and distinguishing features. *Journal of Geophysical Research*, *116*, A02103. https://doi.org/10.1029/2010JA015913

Turner, J. M., Burlaga, L. F., Ness, N. F., & Lemaire, J. F. (1977). Magnetic holes in the solar wind. *Journal of Geophysical Research*, *82*, 1921–1924. https://doi.org/10.1029/JA082i013p01921

Vinogradov, A. A., Vasko, I. Y., Artemyev, A. V., Yushkov, E. V., Petrukovich, A. A., & Zelenyi, L. M. (2016). Kinetic models of magnetic flux ropes observed in the earth magnetosphere. *Physics of Plasmas*, *23*(7), 072901. https://doi.org/10.1063/1.4958319

Winterhalter, D., Neugebauer, M., Goldstein, B. E., Smith, E. J., Bame, S. J., & Balogh, A. (1994), Ulysses field and plasma observations of magnetic holes in the solar wind and their relation to mirror-mode structures, *Journal of Geophysical Research*, *99*, 23371–23381. https://doi.org/10.1029/94JA01977

Xiao, T., Shi, Q. Q., Zhang, T. L., Fu, S. Y., Li, L., Zong, Q. G., et al. (2010). Cluster-C1 observations on the geometrical structure of linear magnetic holes in the solar wind at 1 AU. *Annals of Geophysics*, *28*, 1695–1702. https://doi.org/10.5194/angeo-28-1695-2010

Yao, S. T., Hamrin, M., Shi, Q. Q., Yao, Z. H., Degeling, A. W., Zong, Q. -G., et al. (2020). Propagating and dynamic properties of magnetic dips in the dayside magnetosheath: MMS observations. *Journal of Geophysical Research: Space Physics*, *125*, e2019JA026736. https://doi.org/10.1029/2019JA026736

Yao, S. T., Shi, Q. Q., Guo, R. L., Yao, Z. H., Fu, H.S., Degeling, A. W., et al. (2020b). Kinetic-scale flux rope in the magnetosheath boundary layer. *The Astrophysical Journal*, *897*, 137. https://doi.org/10.3847/1538-4357/ab9620

Yao, S. T., Shi, Q. Q., Li, Z. Y., Wang, X. G., Tian, A. M., Pitkänen, T., et al. (2016). Propagation of small size magnetic holes in the magnetospheric plasma sheet. *Journal of Geophysical Research Space Physics*, *121*, 5510–5519. https://doi.org/10.1002/2016JA022741

Yao, S. T., Shi, Q. Q., Liu, J., Yao, Z. H., Guo, R. L., Ahmadi, N., et al. (2018). Electron dynamics in magnetosheath mirror-mode structures. *Journal of Geophysical Research Space Physics*, *123*, 5561–5570. https://doi.org/10.1029/2018JA025607

Yao, S. T., Shi, Q. Q., Yao, Z. H., Guo, R. L., Zong, Q. G., Wang, X. G., et al. (2019). Electron mirror-mode structure: Magnetospheric multi-scale observations. *The Astrophysical Journal Letters*, *881*(2), L31. https://doi.org/10.3847/2041-8213/ab3398

Yao, S. T., Shi, Q. Q., Yao, Z. H., Li, J. X., Yue, C., Tao, X., et al. (2019). Waves in kinetic-scale magnetic dips: MMS observations in the magnetosheath. *Geophysical Research Letters*, *46*, 523–533. https://doi.org/10.1029/2018GL080696

Yao, S. T., Wang, X. G., Shi, Q. Q., Pitkänen, T., Hamrin, M., Yao, Z. H., et al. (2017). Observations of kinetic-size magnetic holes in the magnetosheath. *Journal of Geophysical Research Space Physics*, *122*. https://doi.org/10.1002/2016JA023858

Yao, S. T., Yue, Z. S., Shi, Q. Q., Degeling, A. W., Fu, H. S., Tian, A. M., et al. (2021). Statistical properties of kinetic-scale magnetic holes in terrestrial space. *Earth and Planetary Physics*, *5*(1), 63–72. https://doi.org/10.26464/epp2021011

Zhang, X. -J., Artemyev, A., Angelopoulos, V., & Horne, R. B. (2017). Kinetics of sub-ion scale magnetic holes in the near-Earth plasma sheet. *Journal of Geophysical Research Space Physics*, *122*, 10304. https://doi.org/10.1002/2017JA024197